Supplementary Information for

Black Carbon Emissions Generally Underestimated in the Global South as Revealed by Globally Distributed Measurements

Yuxuan Ren[1*], Christopher R. Oxford[1], Dandan Zhang[1], Xuan Liu[1,2], Haihui Zhu[1,3], Ann M. Dillner[4], Warren H. White[4], Rajan K. Chakrabarty[1], Sina Hasheminassab[5], David J. Diner[5], Emmie J. Le Roy[1], Joshin Kumar[1], Valerie Viteri[1], Keyao Song[1], Clement Akoshile[6], Omar Amador-Muñoz[7], Araya Asfaw[8], Rachel Ying-Wen Chang[9], Diana Francis[10], Paterne Gahungu[11], Rebecca M. Garland[12,13], Michel Grutter[7], Jhoon Kim[14], Kristy Langerman[15], Pei-Chen Lee[16], Puji Lestari[17], Olga L. Mayol-Bracero[18], Mogesh Naidoo[12], Narendra Nelli[10], Norm O'Neill[19], Sang Seo Park[20], Abdus Salam[21], Bighnaraj Sarangi[18], Yoav Schechner[22], Robyn Schofield[23], Sachchida N. Tripathi[24,25], Eli Windwer[26], Ming-Tsang Wu[27,28], Qiang Zhang[29], Yinon Rudich[26], Michael Brauer[30], and Randall V. Martin[1]

[1]Department of Energy, Environmental & Chemical Engineering, Washington University in St. Louis, St. Louis, Missouri 63130, United States

[2]Scripps Institution of Oceanography, University of California San Diego, San Diego, California 92093, United States

[3]Department of Atmospheric Science, Colorado State University, Fort Collins, Colorado 80521, United States

[4]Air Quality Research Center, University of California Davis, Davis, California 95616, United States

[5]Jet Propulsion Laboratory, California Institute of Technology, Pasadena, California 91109, United States

[6]Department of Physics, University of Ilorin, Ilorin, 240003, Nigeria

[7]Instituto de Ciencias de la Atmósfera y Cambio Climático, Universidad Nacional Autónoma de México, Mexico City, 04510, Mexico

[8]Institute of Geophysics and Space Science, Addis Ababa University, Addis Ababa, 1176, Ethiopia

[9]Department of Physics and Atmospheric Science, Dalhousie University, Halifax, Nova Scotia B3H 4R2, Canada

[10]Environmental and Geophysical Sciences Lab, Earth Science Department, Khalifa University, Abu Dhabi, 127788, United Arab Emirates

[11]Institute of Applied Statistics, University of Burundi, Bujumbura, BP1550, Burundi

[12]Council for Scientific and Industrial Research, Pretoria, 0001, South Africa

[13]Department of Geography, Geo-Informatics and Meteorology, University of Pretoria, Pretoria, 0002, South Africa

[14]Department of Atmospheric Sciences, Yonsei University, Seoul, 03722, Republic of Korea

[15]Department of Geography, Environmental Management and Energy Studies, University of Johannesburg, Johannesburg, 2006, South Africa

[16]Department of Public Health, National Cheng Kung University, Tainan, 701, Taiwan

[17]Faculty of Civil and Environmental Engineering, Bandung Institute of Technology, Bandung, 40132, Indonesia

[18]Department of Environmental Science, University of Puerto Rico, Puerto Rico, 00931, United States

[19]Dépt de géomatique appliquée , Université de Sherbrooke, Sherbrooke, Québec, J1K 2R1, Canada

[20]Department of Urban and Environmental Engineering, Ulsan National Institute of Science and Technology, Ulsan, 44919, Republic of Korea

[21]Department of Chemistry, University of Dhaka, Dhaka, 1000, Bangladesh

[22]Department of Electrical Engineering, Technion Israel Institute of Technology, Haifa, 3200003, Israel

[23]School of Geography, Earth and Atmospheric Sciences, University of Melbourne, Melbourne, 3010, Australia

[24]Department of Civil Engineering, Indian Institute of Technology Kanpur, Kanpur, 208016, India

[25]Department of Sustainable Energy Engineering, Indian Institute of Technology Kanpur, Kanpur, 208016, India

[26]Department of Earth and Planetary Sciences, Weizmann Institute of Science, Rehovot, 76100, Israel

[27]Department of Family Medicine, Kaohsiung Medical University Hospital, Kaohsiung Medical University, Kaohsiung, 807, Taiwan

[28]PhD Program in Environmental and Occupational Medicine, Kaohsiung Medical University, Kaohsiung, 807, Taiwan

[29]School of Environment, Tsinghua University, Beijing, 100084, China

[30]School of Population and Public Health, University of British Columbia, Vancouver, British Columbia V6T 1Z3, Canada

[*]Email: ren.yuxuan@wustl.edu

Contents of this file

This Supplementary Information contains Text S1 to S5, Tables S1 to S4, and Figures S1 to S10.

Text S1. Statistics Calculation

We mainly use the line of best fit (y), coefficient of determination (r^2), normalized mean bias (NMB, Eq. 1), and normalized mean difference (NMD, Eq. 2) to evaluate simulated BC concentrations (C_{sim}) using coincident measurements (C_{meas}) across a total of N SPARTAN sites. The r^2 value reflects the consistency in the relative spatial distribution between simulations and measurements, while the slope indicates whether the model systematically overestimates or underestimates the measurements.

$$NMB = \frac{\sum_{i=1}^{N}(C_{sim,i} - C_{meas,i})}{\sum_{i=1}^{N} C_{meas,i}} \quad (1)$$

$$NMD = \frac{\sum_{i=1}^{N}|C_{sim,i} - C_{meas,i}|}{\sum_{i=1}^{N} C_{meas,i}} \quad (2)$$

where $C_{sim,i}$ is the simulated BC concentration at SPARTAN site i, $C_{meas,i}$ is the measured BC concentration at the same site, and $|C_{sim,i} - C_{meas,i}|$ is the absolute difference between the simulated and measured concentrations.

Text S2. Evaluation Using Complementary Measurements

In addition to the robust evaluation based on long-term measurements from globally distributed SPARTAN sites, we extend our analysis by incorporating data from other available networks and individual studies ("Methods" section). Figure 1 and Figure S9 present evaluation results using the original and the relaxed data screening criteria, which require a minimum sampling duration of six months and two months, respectively. The evaluation with complementary measurements generally supports similar conclusions as those derived from SPARTAN, showing overall consistency in developed regions while highlighting discrepancies in the Global South. Notably, with the original data screening criteria, the median simulated-to-measured ratio is 0.44 across five sites in South America and 0.25 across six sites in Africa. While emission evaluations in the Global South remain limited, several site-specific studies also indicate underestimation in simulations. For example, simulated BC concentrations using three different emission inventories were consistently lower than measured values

at a rural site in India, with a median simulated-to-measured ratio of 0.59[1]. Similarly, in Tacna, Peru, simulated BC concentrations were found to be an order of magnitude lower than ground-based measurements[2]. These pronounced discrepancies reveal the challenges in accurately representing BC emissions in existing inventories across the Global South.

Unlike SPARTAN, which maintains consistency across all globally distributed sites and ensures robustness for evaluation, complementary datasets are compiled from diverse sources and exhibit inherent variability in instrumentation, sampling objectives, and sampling schemes. Despite applying a careful data screening process, we acknowledge the uncertainties associated with these variations and, therefore, primarily focus our discussion on SPARTAN data.

Text S3. Representativeness Bias

Differences in representativeness between measurements and simulations arise from comparing a point measurement with an area average, magnified by the tendency for measurements to be in locations with elevated BC concentrations[3-5]. To examine this potential bias, we perform GCHP sensitivity simulations at the finest available meteorological resolution of C720 (~12 km) and compare BC concentrations with those from simulations at C360 (~25 km) resolution in 2022, the year in which archival began of the GEOS-FP C720 meteorological data. A full-year simulation at C720 would be computationally prohibitive. However, a high level of consistency is found between BC concentrations in the C360 and C720 simulations (Figure S10), indicating that comparing BC simulations at approximately 25 km resolution with point measurements would yield similar results as using a 12 km simulation. The most prominent exception is for Beijing in January, where and when the C720 has BC concentrations that are 22% lower than at C360, partially explaining the anomaly apparent in Figure 2. Moreover, SPARTAN stations are mostly located on rooftops with a mean height of 17 m, which increases their spatial fetch (Table S3), generally reducing differences between volume-averaged modeled concentrations and point measurements.

Text S4. Fe Correction

In addition to muliple methods for measuring aerosol absoprtion, SPARTAN filters are analyzed for elemental composition by X-ray fluorescence (XRF). The total Fe content is determined with high reliability, with measurement procedures and quality assurance detailed in Liu et al.[6]. Fe serves as a tracer for absorbing dust and has a distinct association with absorption. White et al.[7] examined Fe's interference on BC determination using HIPS and derived the following relationship using 10 years of measurements from IMPROVE:

$$b_{abs} = A \times M_{BC,corrected} + B \times M_{Fe} \quad (3)$$

where b_{abs} is the absorption coefficient determined by HIPS, $M_{BC,\ corrected}$ is the BC concentration corrected for dust interference on absorption, and M_{Fe} is the total Fe content measured by XRF. The coefficients A = 10.2 m^2/g BC and B = 6.6 m^2/g Fe represent the MAC estimates for BC and Fe, respectively.

Text S5. HIPS Methodology

HIPS independently measures both transmittance (t) using an integrating plate and reflectance (r) using a sphere positioned on the unexposed side of the filter using He-Ne laser light (633 nm)[7]. The reflectance measurement accounts for pre-sampling transmittance and additionally supplies a correction for backscattering by sampled particles, thus accounting for filter loading effects (i.e., nonlinear decrease in attenuation as more absorbing particles accumulate on the filter). The absorption coefficient (b_{abs}) is determined as follows:

$$b_{abs} = \frac{A}{V} \ln\left(\frac{1-r}{t}\right) \quad (4)$$

The absorption coefficient is then converted to BC mass using the mass absorption cross section (MAC). The MAC for HIPS has been rigorously evaluated within the U.S. Interagency Monitoring of PROtected Visual Environments (IMPROVE) network. This evaluation involves parallel sampling on both Teflon and quartz filters, where the

Teflon filter is analyzed for absorption using HIPS following the same methodology as in SPARTAN, while the quartz filter is analyzed for elemental carbon (EC) using the IMPROVE thermal optical reflectance (TOR) method[8,9]. Using EC mass as the reference, the MAC is calculated as:

$$MAC = \frac{b_{abs}}{M_{EC}} \tag{5}$$

Therefore, BC mass from SPARTAN HIPS can be determined as:

$$M_{BC} = \frac{b_{abs}}{MAC} \tag{6}$$

To account for multiple scattering effects (i.e., optical interactions between absorbing particles and the multiple-scattering filter substrate), HIPS applies a theory-based calibration model with parameters derived from field blank measurements[7]. Briefly, a linear regression of field blanks provides an intercept a_0 and slope a_1, which transform raw reflectance R and transmittance T values into the field blank corrected values:

$$\mathrm{r} = -\frac{a_1 R}{a_0},\ t = \frac{T}{a_0} \tag{7}$$

This correction method ensures that field blanks exhibit zero absorption, effectively mitigating multiple scattering effects. To ensure accuracy, at least 40 field blanks from the same Teflon filter batch are used in the calibration process. Additionally, unlike conventionally used optically thick quartz- or glass-fiber filters, the Teflon filters used in SPARTAN have considerably lower surface areas for physical adsorption and exhibit minimal absorption of gas-phase organic carbon. Additionally, Teflon filters introduce much less extraneous scattering to the analyzed matrix of collected particles and the filter substrate.

Tables

Table S1. Sampling information and BC concentration (μg/m^3) for SPARTAN sites used in this study.

Site	Start Date	Most Recent Sample Date	Sampling Seasons[a]	Start Date for MAIA Sites[b]	*N*[c]	Mean (Median)	Standard Error
Abu Dhabi	4/26/2019	12/23/2023	DJF, MAM, JJA, SON		113	2.7 (2.7)	0.11
Addis Ababa	12/7/2022	12/27/2023	DJF, MAM, JJA, SON	12/7/2022	116	4.8 (4.5)	0.19
Bandung	9/6/2019	7/11/2021	DJF, MAM, JJA, SON		23	3.7 (3.9)	0.20
Beijing	3/24/2020	11/28/2023	DJF, MAM, JJA, SON	8/30/2022	153	1.4 (1.3)	0.090
Bujumbura	12/9/2022	12/26/2023	DJF, MAM, JJA, SON		18	3.7 (3.2)	0.40
Dhaka	8/11/2020	10/7/2023	MAM, JJA, SON		52	5.6 (5.4)	0.86
Fajardo	3/18/2021	12/24/2023	DJF, MAM, JJA, SON		34	0.11 (0.083)	0.017
Haifa	2/16/2022	6/17/2023	DJF, MAM, JJA, SON	2/16/2022	143	0.85 (0.63)	0.10
Halifax	6/14/2019	10/24/2023	DJF, MAM, JJA, SON		112	0.23 (0.21)	0.015
Ilorin	7/13/2019	12/1/2021	DJF, MAM, JJA, SON		36	3.0 (2.2)	0.61
Johannesburg	4/7/2022	12/28/2023	DJF, MAM, JJA, SON	4/7/2022	168	2.4 (2.3)	0.18
Kanpur	7/14/2021	5/24/2022	DJF, MAM, JJA		14	3.8 (3.0)	0.73
Kaohsiung	8/20/2022	12/29/2023	DJF, MAM, JJA, SON	8/20/2022	123	1.3 (1.4)	0.12
Melbourne	8/9/2022	12/28/2023	DJF, MAM, JJA, SON		34	0.43 (0.32)	0.061
Mexico City	2/26/2021	12/24/2023	DJF, MAM, JJA, SON		52	2.1 (2.0)	0.11
Pasadena	11/9/2021	11/15/2023	DJF, MAM, JJA, SON	11/9/2021	233	0.47 (0.44)	0.030
Pretoria	10/22/2020	12/27/2023	DJF, MAM, JJA, SON	4/15/2021	233	2.1 (2.0)	0.24
Rehovot	7/2/2020	6/7/2023	DJF, MAM, JJA, SON	11/5/2021	178	1.2 (1.0)	0.11
Seoul	9/11/2020	12/30/2023	DJF, MAM, JJA, SON		65	1.2 (1.1)	0.094
Sherbrooke	8/29/2019	6/21/2023	DJF, MAM, JJA, SON		67	0.36 (0.28)	0.049
Taipei	1/27/2022	12/31/2023	DJF, MAM, JJA, SON	1/27/2022	218	0.83 (0.75)	0.040
Ulsan	10/28/2021	12/23/2023	DJF, MAM, JJA, SON		92	0.78 (0.74)	0.043

[a] DJF includes December, January, and February; MAM includes March, April, and May; JJA includes June, July, and August; SON includes September, October, and November.

[b] These sites began using the MAIA sampling protocol on the specified date.

[c] *N* is the number of samples from each site included in this study.

Table S2. Recent laboratory and field-measured mass absorption cross section (MAC, m^2/g) values across different regions and combustion sources.

Source	b_{abs} via	M_{BC} via	Wavelength (nm)	Measured MAC (m^2/g)	MAC at 633 nm (m^2/g)[a]	Reference
Fresh emitted BC	NaN	NaN	550	7.5 ± 1.2	6.52 ± 1.04	Bond and Bergstrom[10]
Fresh emitted BC	NaN	NaN	550	8	6.95	Liu et al.[11]
Arctic background	Aethalometer 31 and 33	COSMOS[b]	590	11.7	10.9	Singh et al.[12]
US background	HIPS	Thermal/Optical Carbon Analyzer	633	10.2	10.2	White et al.[7]
Biofuel stoves	PAX[c]	Sunset OC/EC Analyzer	870	5.84	8.03	Wu et al.[13]
Cookstoves	PAX	SP2[d]	405	13.7	8.77	Saliba et al.[14]
Diesel trucks	PAX	Sunset OC/EC Analyzer	870	5.275	7.25	Wu et al.[13]
Marine diesel engine	CAPS Pmssa[e]	SP2	780	7.8 ± 1.8	9.61 ± 2.22	Corbin et al.[15]
Non-road mobile machinery	PAX	Sunset OC/EC analyzer	550	11.5 ± 3.4	9.99 ± 2.95	Wu et al.[16]
Solid and liquid fossil fuel sources	Thermal/Optical Carbon Analyzer	Thermal/Optical Carbon Analyzer	632	8.00 ± 3.12	7.99 ± 3.12	Yan et al.[17]
Biogenic and fossil fuel sources	PAX	Sunset OC/EC Analyzer	520	9.0 ± 3.7	7.39 ± 3.04	Olson et al.[18]

[a] For direct comparison, we adjust the MAC values to 633 nm, the wavelength used in Hybrid Integrating Plate/Sphere (HIPS) measurements in SPARTAN. This adjustment assumes that MAC varies inversely with wavelength and that the particles are small relative to the wavelength[10].

[b] Continuous Soot Monitoring System.

[c] Photoacoustic Extinctiometer.

[d] Single Particle Soot Photometer.

[e] Cavity Attenuation Phase Shift PM SSA Monitor.

Table S3. Location information of SPARTAN sites used in this study.

Site	Host Institute	Latitude	Longitude	Rooftop Height (m)
Abu Dhabi	Masdar Institute	24.44	54.62	27
Addis Ababa	Addis Ababa University	9.01	38.82	3
Bandung	Institute of Technology Bandung	-6.89	107.61	30
Beijing	Tsinghua University	40.00	116.33	9
Bujumbura	University of Burundi	-3.38	29.38	12
Dhaka	Dhaka University	23.73	90.40	22
Fajardo	Cabezas de San Juan Nature Reserve	18.38	-65.62	4
Haifa	Technion Israel Institute of Technology	32.78	35.02	32
Halifax	Dalhousie University	44.64	-63.59	13
Ilorin	Ilorin University	8.48	4.67	11
Johannesburg	University of Johannesburg	-26.18	28.00	11
Kanpur	Indian Institute of Technology Kanpur	26.51	80.23	8
Kaohsiung	Kaohsiung Medical University	22.65	120.31	15
Melbourne	University of Melbourne	-37.80	144.96	57
Mexico City	Universidad Nacional Autónoma de México	19.33	-99.18	16
Pasadena	Jet Propulsion Laboratory	34.20	-118.17	15
Pretoria	Council for Scientific and Industrial Research	-25.76	28.28	13
Rehovot	Weizmann Institute	31.91	34.81	16
Seoul	Yonsei University	37.56	126.93	25
Sherbrooke	Sherbrooke University	45.38	-71.93	9
Taipei	National Taiwan University	25.04	121.50	10
Ulsan	Ulsan National Institute of Science and Technology	35.58	129.19	12

Table S4. Sector definitions for CEDS v2, EDGAR v6.1, and HTAP v3. Multiple categories are lumped into aggregate sectors in CEDS.

	CEDS v2	EDGAR v6.1	HTAP v3
Energy production	Electricity-public	Power industry	Energy
	Electricity-autoproducer	Fuel exploitation	
	Heat-production	Oil refineries and Transformation industry	
	Other-transformation	Fossil fuel fires	
	Fugitive-solid-fuels		
	Fugitive-petr-and-gas		
	Fugitive-other-energy		
	Fossil-fuel-fires		
Industry	Ind-Comb-Iron-steel	Combustion for manufacturing	Industry
	Ind-Comb-Non-ferrous-metals	Chemical processes	Fugitive
	Ind-Comb-Chemicals	Iron and steel production	
	Ind-Comb-Pulp-paper	Non-ferrous metals production	
	Ind-Comb-Food-tobacco		
	Ind-Comb-Non-metallic-minerals		
	Ind-Comb-Construction		
	Ind-Comb-transpequip		
	Ind-Comb-machinery		
	Ind-Comb-mining-quarrying		
	Ind-Comb-wood-products		
	Ind-Comb-textile-leather		
	Ind-Comb-other		
	Other-unspecified		
	Cement-production		
	Lime-production		
	Other-minerals		
	Chemical-industry		
	Metal-production		
	Pulp-and-paper-food-beverage-wood		
	Other-process-emissions		
	Other-in-total		
Transportation	Road	Road transportation	Road Transport
	Rail	Railways, pipelines, off-road transport	Brake and Tyre wear
	Domestic-navigation		Domestic shipping
	Other-transp		Other ground transport

Residential, commercial, other	Residential Commercial-institutional Agriculture-forestry-fishing	Energy for buildings	Residential
Solvents	Degreasing-Cleaning Other-product-use Paint-application Chemical-products-manufacture-processing	Solvents and products use	Solvents
Agriculture	Manure-management Soil-emissions Agriculture-other Rice-Cultivation Enteric-fermentation	Manure management Agricultural soils Agricultural waste burning Enteric fermentation	Agricultural waste burning Agriculture_livestock Agriculture_crops
Waste	Solid-waste-disposal Other-waste-handling Waste-incineration Wastewater-handling	Solid waste incineration Solid waste landfills Wastewater handling	Waste
Shipping	International shipping Oil_Tanker_Loading	Shipping	International Shipping
Aviation		Aviation climbing&descent Aviation cruise Aviation landing&takeoff	Domestic Aviation International Aviation

Table S5. Sampling information and BC concentration for other individual measurements referenced in this study. Mass absorption cross section (MAC, m^2/g) values at 880 nm and estimated values at 633 nm are provided for measurements using the aethalometer (AE) when available.

Country	Site	Latitude	Longitude	Location Type	Instrument	MAC at 880 nm (m^2/g)	MAC at 633 nm (m^2/g)[a]	Sampling Period	M_{BC} ($\mu g/m^3$)	Reference
Argentina	Buenos Aires	-34.56	-58.51	suburban	AE42	16.6	23.1	Nov 2014 to Mar 2016	3.18	Resquin et al.[19]
Brazil	Londrina	-23.31	-51.11	suburban	AE42	16.6	23.1	Aug 2014 to Jul 2018	0.73	Targino et al.[20]
Bolivia	La Paz	-16.50	-68.13	urban	AE33	7.77	10.8	Jan to Jun, 2018	1.6	Mardoñez-Balderrama et al.[21]
Ivory Coast	Lamto	6.22	-5.03	rural	AE31	16.6	23.1	Jan 2015 to May 2017	1.4	Kouassi et al.[22]
Mexico	Monterrey	25.75	-100.26	urban	AE33	16.6	23.1	Jan to Dec, 2016	2.46	Peralta et al.[23]
Peru	Hyo	-12.04	-75.32	rural	AE33	7.77	10.8	May 2022 to Oct 2023	0.65	Villalobos-Puma et al.[24]
Peru	Tacna	-18.02	-70.25	urban	PAX[c]	NaN	6.51	Nov 2019 to Sep 2021	0.745	Liñán-Abanto et al.[2]
Chile[b]	Las Encinas[b]	-38.75	-72.62	urban	SIMCA[d]	NaN	NaN	Jul, Nov, and Dec, 2019	0.905	Reyes et al.[25]
Colombia[b]	Barranquilla[b]	10.99	74.79	urban	AE33	7.77	10.8	May to Jun, 2019	1.04	Blanco-Donado et al.[26]
South Africa[b]	Kwadela[b]	-26.46	29.66	semi-rural	AE31	16.6	23.1	Feb to Apr, 2015	0.66	Xulu et al.[27]
Rwanda	Kigali	-1.96	30.06	urban	BC1060[e]	NaN	NaN	Jan to Dec, 2020	7.8	Kalisa and Adams[28]
Mozambique	Manhiça	-25.41	32.81	semi-rural	Sunset OC/EC Analyzer	NaN	NaN	2014 to 2015	0.9	Curto et al.[29]
Cotonou	Benin	6.35	-2.43	urban	Thermal/Optical Carbon Analyzer	NaN	NaN	Feb 2015 to Mar 2017	2	Djossou et al.[30]
Ivory Coast	Abidjan	5.33	-4.02	urban	Thermal/Optical Carbon Analyzer	NaN	NaN	Feb 2015 to Mar 2017	7	Djossou et al.[30]

[a] In AE studies, MAC measurements at 880 nm are typically used to calculate BC concentrations[19]. For direct comparison, we adjust the MAC values to 633 nm, the wavelength used in Hybrid Integrating Plate/Sphere (HIPS) measurements in SPARTAN. This adjustment assumes that MAC varies inversely with wavelength and that the particles are small relative to the wavelength[10].

[b] These measurements are included only in the additional complementary dataset with a relaxed sampling length criterion of two months.

[c] Photoacoustic Extinctiometer.

[d] Absorption Coefficient Measurement System.

[e] Portable Black Carbon Monitors.

Figures

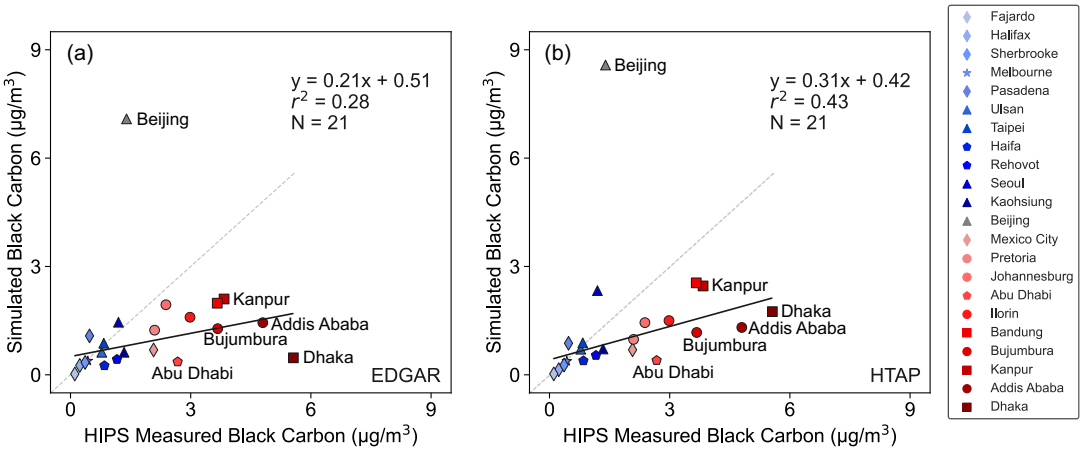

Figure S1. Sensitivity test using alternative emission inventories. Annual mean BC concentrations across SPARTAN sites (2019–2023) are compared with those from 2019 GCHP simulations using different inventories at C360 resolution (~25 km). (a) EDGAR and (b) HTAP. Annotations include the line of best fit (y), coefficient of variation (r^2), and number of comparison points (N). The lowest half of the measured concentrations are indicated in blue and the upper half in red. The Beijing site, marked in grey, is excluded from statistical calculations due to anomalies in its emissions estimates. Symbols indicate different regions (diamonds for North America, star for Australia, triangles for East Asia, pentagons for the Middle East, circles for Africa, and squares for South Asia).

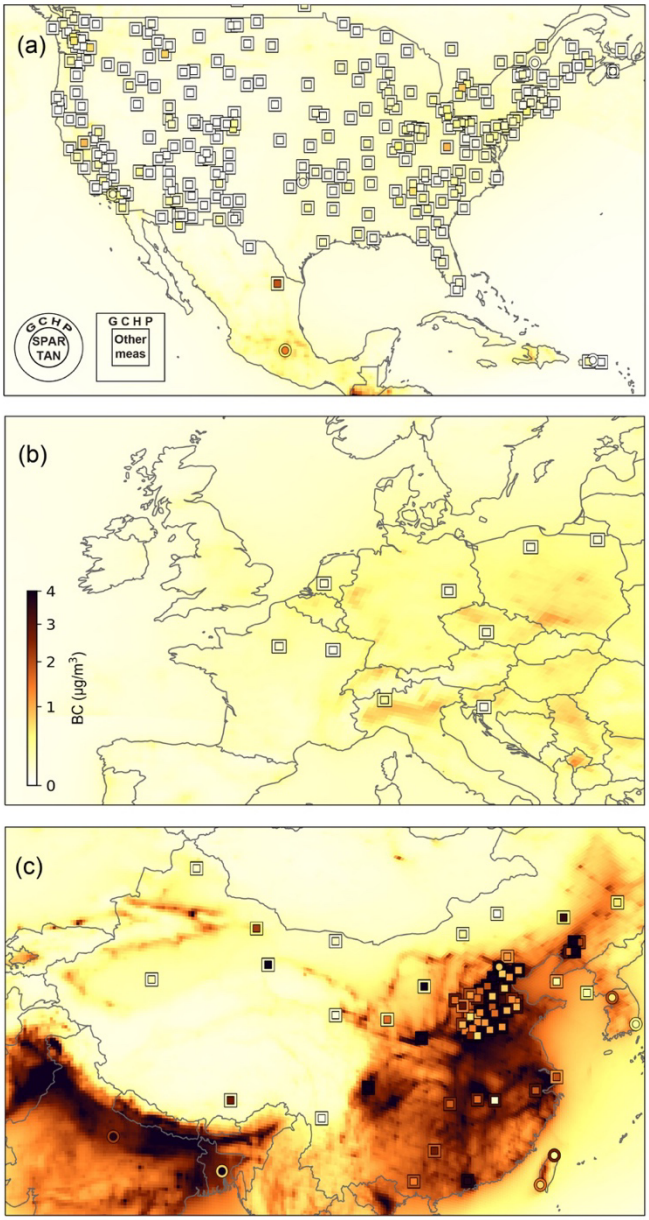

Figure S2. Black carbon (BC) concentrations from measurements and simulation using a widely-used emission inventory across different regions. (a) North America, (b) Europe, and (c) East Asia. SPARTAN and additional measurements are represented by colored circles and squares, respectively, surrounded by concentric circles and squares indicating local GCHP concentrations using the CEDS inventory. A GCHP C360 (~25 km) simulation using the CEDS inventory is in the background. Complementary measurements are sourced from the Chemical Speciation Network (CSN) and the Interagency Monitoring of PROtected Visual Environments (IMPROVE) network in the US, the National Air Pollution Surveillance Network (NAPS) in Canada, the European Monitoring and Evaluation Programme (EMEP) in Europe, the China Atmosphere Watch Network (CAWNET)[31] and Dao et al.[32] in China. The original data screening scheme with a six-month sampling length criterion is used here.

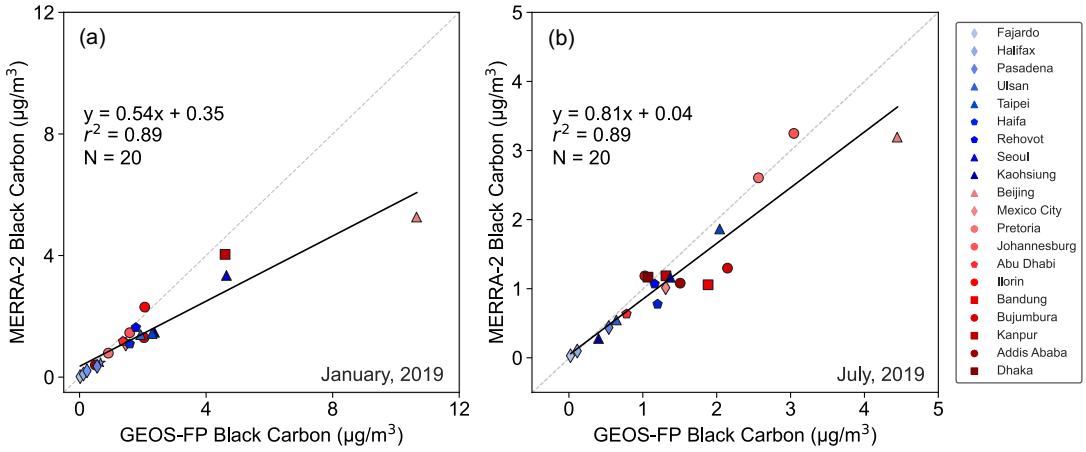

Figure S3. Sensitivity test using alternative meteorology. Mean simulated black carbon (BC) concentrations from 2019 GCHP simulations using GEOS-FP and MERRA-2 meteorology at C180 resolution (~50 km) are compared across SPARTAN sites. (a) January and (b) July. Annotations include the line of best fit (y), coefficient of variation (r^2), and number of comparison points (N). Symbols indicate different regions (diamonds for North America, triangles for East Asia, pentagons for the Middle East, circles for Africa, and squares for South Asia).

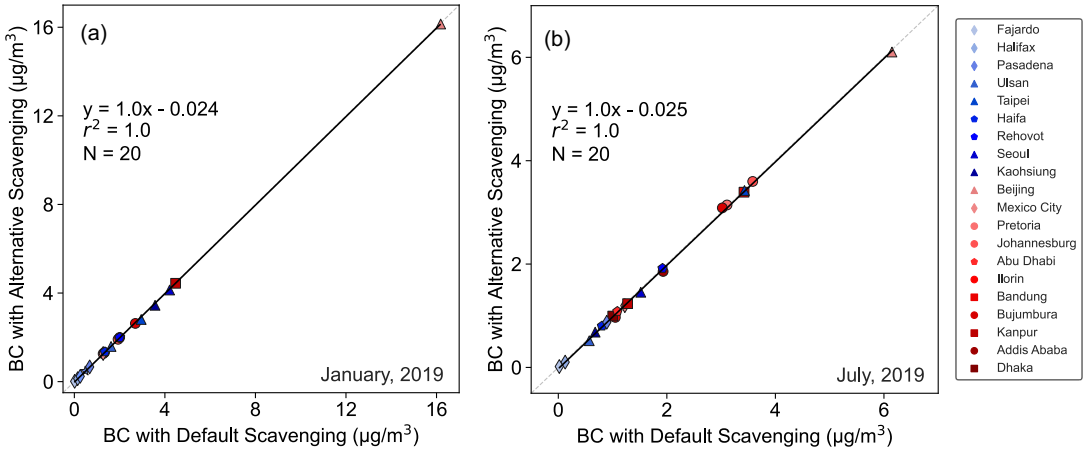

Figure S4. Sensitivity test using alternative wet deposition scheme. Mean simulated black carbon (BC) concentrations from 2019 GCHP simulations using alternative scavenging at C360 resolution (~25 km) are compared across SPARTAN sites. (a) January and (b) July. Annotations include the line of best fit (y), coefficient of variation (r^2), and number of comparison points (N). Symbols indicate different regions (diamonds for North America, triangles for East Asia, pentagons for the Middle East, circles for Africa, and squares for South Asia).

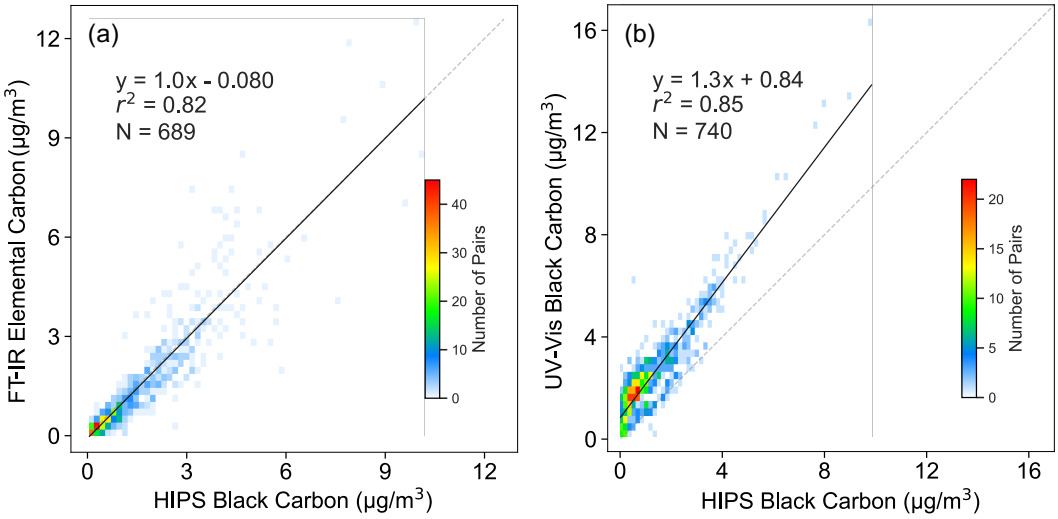

Figure S5. Inter-comparison of black carbon (BC) measurements within SPARTAN. BC concentrations measured by HIPS, FT-IR, and UV-Vis are compared. (a) HIPS vs FT-IR and (b) HIPS vs UV-Vis. Annotations include the line of best fit (y), coefficient of variation (r^2), and number of comparison points (N).

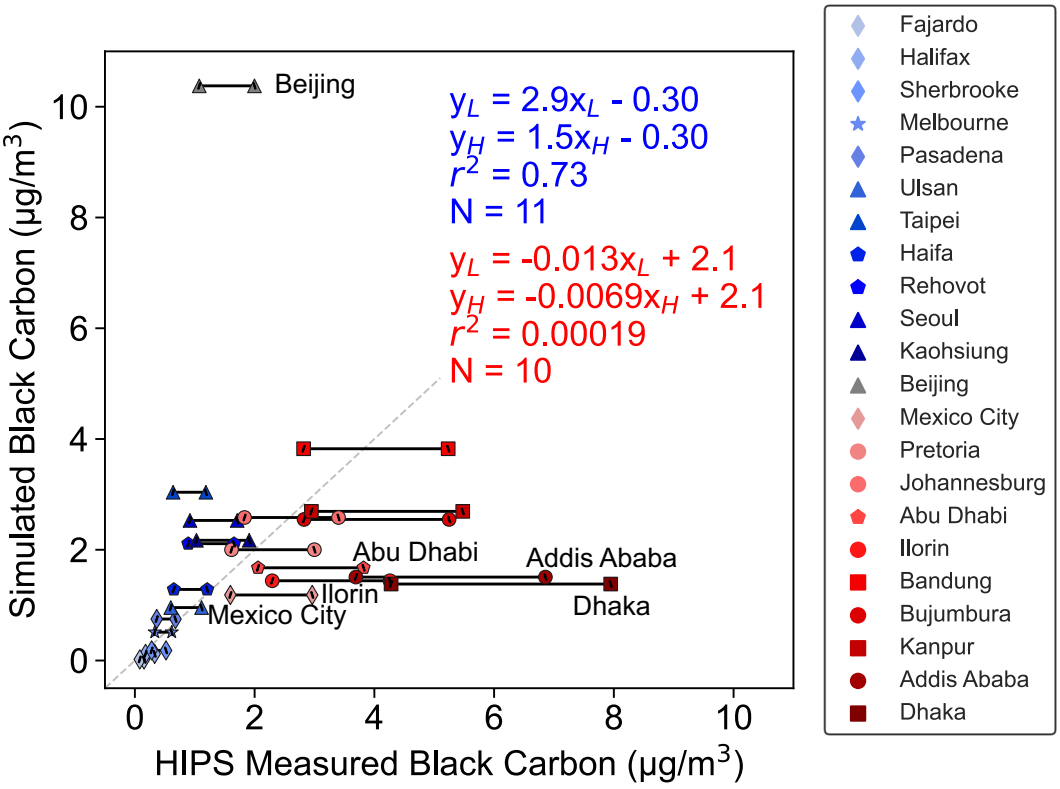

Figure S6. Sensitivity test using mass absorption cross section (MAC) uncertainty range of 7 m^2/g to 13 m^2/g. Annual mean BC concentrations across SPARTAN sites (2019–2023) are compared with those from the 2019 GCHP simulations. Annotations include the line of best fit (y), coefficient of variation (r^2), and number of comparison points (N). A MAC of 7 m^2/g is represented by rightmost markers filled with a backward slash and a line of best fit (y_H) indicating higher BC concentrations, while a MAC of 13 m^2/g is represented by leftmost markers filled with a forward slash and a line of best fit (y_L) indicating lower BC concentrations. The lowest half of the measured concentrations are indicated in blue and the upper half in red. The Beijing site, marked in grey, is excluded from statistical calculations due to anomalies in its emissions estimates. Symbols indicate different regions (diamonds for North America, star for Australia, triangles for East Asia, pentagons for the Middle East, circles for Africa, and squares for South Asia).

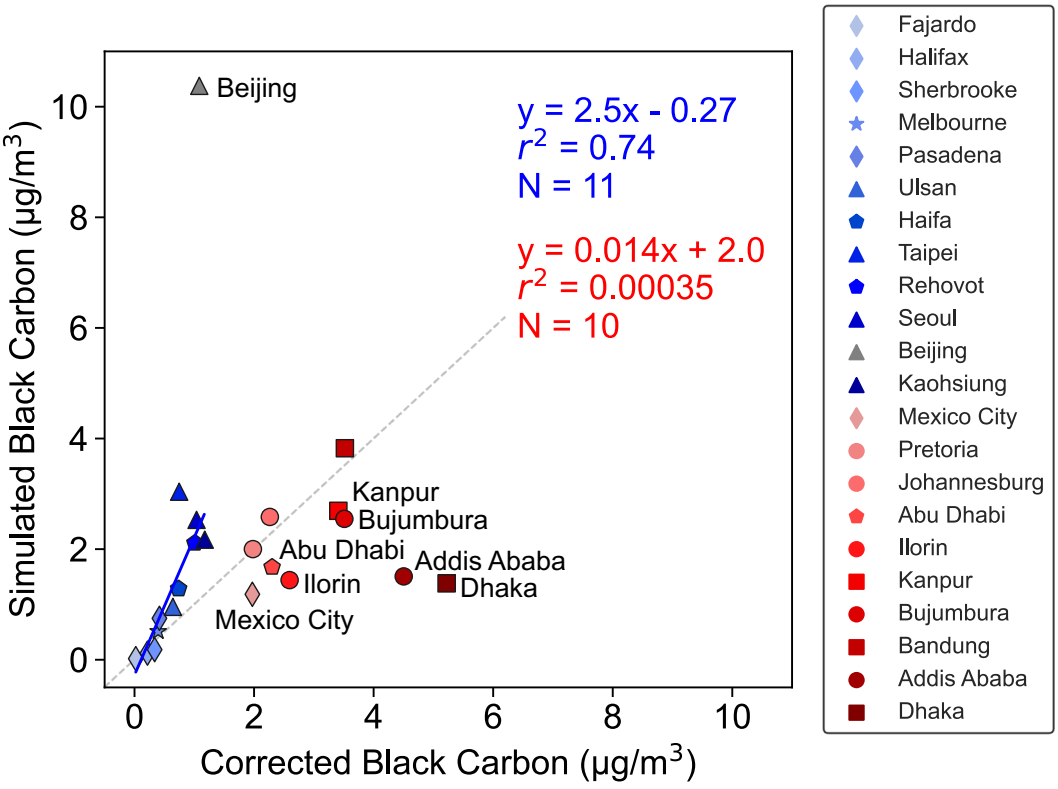

Figure S7. Effect of dust interference on black carbon (BC) measurements. Annual mean BC concentrations across SPARTAN sites (2019–2023) are adjusted for dust interference and compared with those from the 2019 GCHP simulation. Annotations include the line of best fit (y), coefficient of variation (r^2), and number of comparison points (N). The lowest half of the measured concentrations are indicated in blue and the upper half in red. The Beijing site, marked in grey, is excluded from statistical calculations due to anomalies in its emissions estimates. Symbols indicate different regions (diamonds for North America, star for Australia, triangles for East Asia, pentagons for the Middle East, circles for Africa, and squares for South Asia).

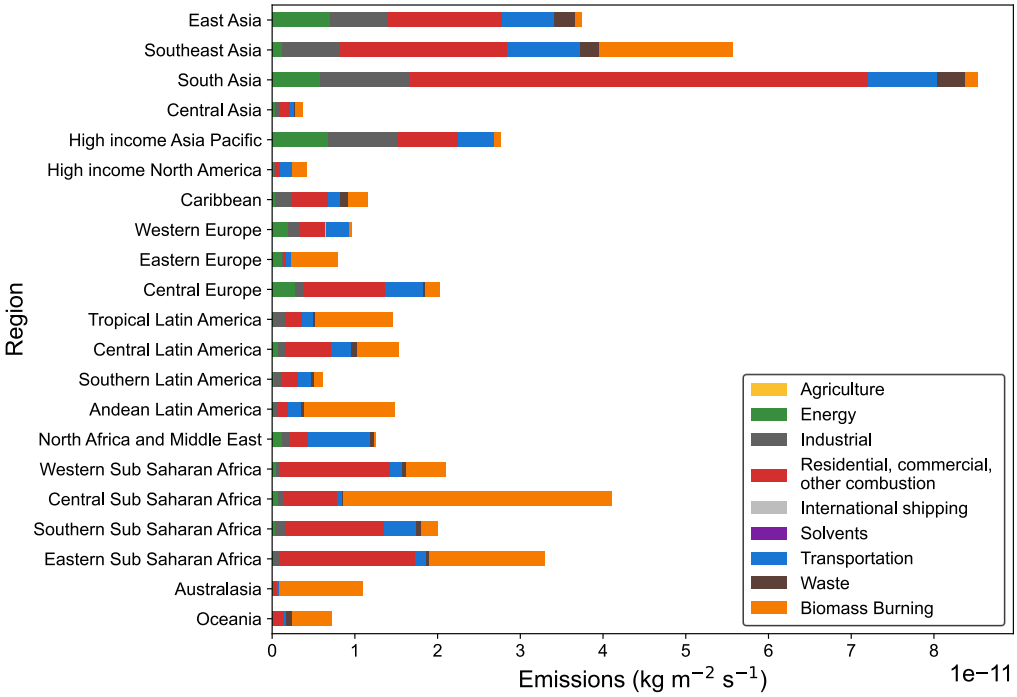

Figure S8. Black carbon (BC) emissions by source sector. BC emissions across 21 global regions are shown by source sector, based on the CEDS v2 and GFED v4.1s emission inventories in 2019. Colored segments within each bar represent contributions from individual sectors.

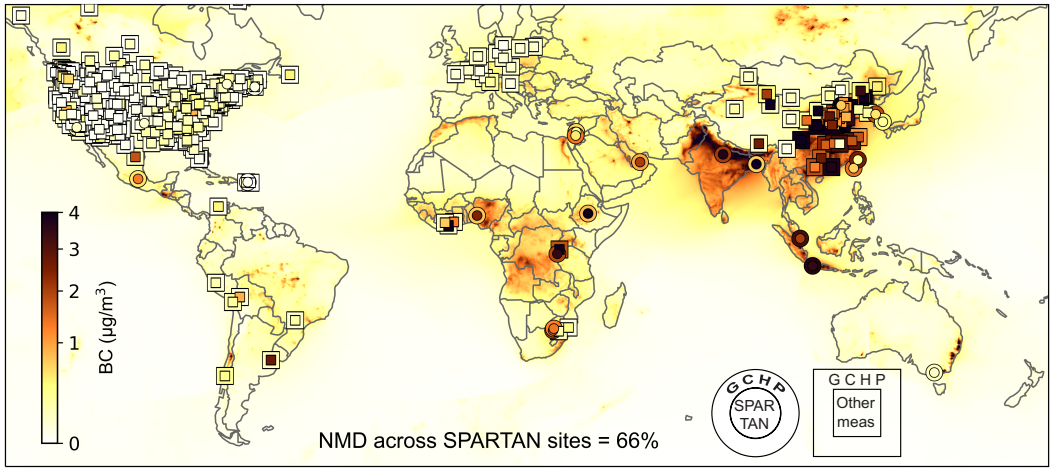

Figure S9. Global black carbon (BC) distribution using relaxed data screening scheme. This map shows ground-level BC from SPARTAN measurements over 2019−2023, complementary measurements using relaxed data screening scheme with a two-month sampling length criterion from adjacent years, and a GCHP simulation using the CEDS emission inventory for 2019. SPARTAN and additional measurements are represented by colored circles and squares, respectively, surrounded by concentric circles and squares indicating local coincident GCHP simulated concentrations. The GCHP simulation is in the background. The inset value is the normalized mean difference (NMD) across SPARTAN sites. Complementary measurements are sourced from the Chemical Speciation Network (CSN) and the Interagency Monitoring of PROtected Visual Environments (IMPROVE) network in the US, the National Air Pollution Surveillance Network (NAPS) in Canada, the European Monitoring and Evaluation Programme (EMEP) in Europe, the China Atmosphere Watch Network (CAWNET)[31] and Dao et al.[32] in China; additional data, primarily covering Africa, South America, and South Asia, are referenced from individual studies[2,19-30].

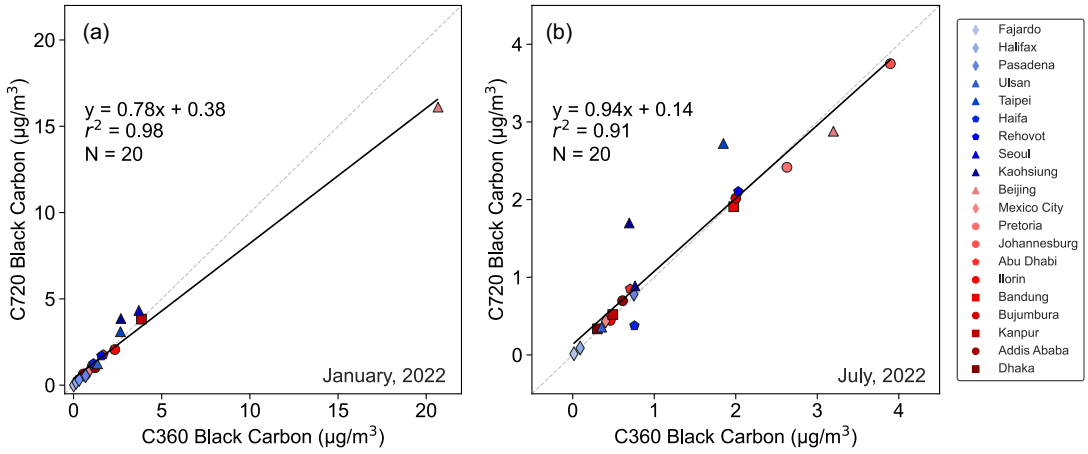

Figure S10. Sensitivity test using model resolution. Mean simulated black carbon (BC) concentrations from 2019 GCHP simulations using the CEDS inventory at C360 (~25 km) and C720 (~12 km) in 2022 are compared across SPARTAN sites. (a) January and (b) July. Annotations include the line of best fit (y), coefficient of variation (r^2), and number of comparison points (N). Symbols indicate different regions (diamonds for North America, triangles for East Asia, pentagons for the Middle East, circles for Africa, and squares for South Asia).

Supplementary References

1. Gadhavi, H. S. et al. Evaluation of black carbon emission inventories using a Lagrangian dispersion model – a case study over southern India. *Atmos. Chem. Phys.* **15,** 1447–1461 (2015).
2. Liñán-Abanto, R. N. et al. Black carbon in a city of the Atacama Desert before and after the start of the COVID-19 lockdown: ground measurements and MERRA-2 reanalysis. *Remote Sens.* **15,** 4702 (2023).
3. Gilardoni, S., Vignati, E. & Wilson, J. Using measurements for evaluation of black carbon modeling. *Atmos. Chem. Phys.* **11**, 439–455 (2011).
4. Swall, J. L. & Foley, K. M. The impact of spatial correlation and incommensurability on model evaluation. *Atmos. Environ.* **43,** 1204–1217 (2009).
5. Wang, R. et al. Spatial representativeness error in the ground-level observation networks for black carbon radiation absorption. *Geophys. Res. Lett.* **45,** 2106–2114 (2018).
6. Liu, X. et al. Elemental characterization of ambient particulate matter for a globally distributed monitoring network: methodology and implications. *Environ. Sci. Technol. Air* **1,** 283–293 (2024).
7. White, W. H., Trzepla, K., Hyslop, N. P. & Schichtel, B. A. A critical review of filter transmittance measurements for aerosol light absorption, and calibration for a decade of monitoring on PTFE membranes. *Aerosol Sci. Tech.* **50,** 984–1002 (2016).
8. Chow, J. C., Watson, J. G., Crow, D., Lowenthal, D. H. & Merrifield, T. Comparison of IMPROVE and NIOSH carbon measurements. *Aerosol Sci. Tech.* **34,** 23–34 (2001).
9. Chow, J. C. et al. The IMPROVE-A temperature protocol for thermal/optical carbon analysis: maintaining consistency with a long-term database. *J. Air & Waste Manage. Assoc.* **57,** 1014–1023 (2007).
10. Bond, T. C. & Bergstrom, R. W. Light absorption by carbonaceous particles: an investigative review. *Aerosol Sci. Tech.* **40,** 27–67 (2006).
11. Liu, F. et al. Review of recent literature on the light absorption properties of black carbon: refractive index, mass absorption cross section, and absorption function. *Aerosol Sci. Tech.* **54,** 33–51 (2020).
12. Singh, M. et al. Mass absorption cross section of black carbon for Aethalometer in the Arctic. *Aerosol Sci. Tech.* **58,** 536–553 (2024).
13. Wu, B. et al. Mass absorption cross-section of black carbon from residential biofuel stoves and diesel trucks based on real-world measurements. *Sci. Total Environ*. **784,** 147225 (2021).
14. Saliba, G. et al. Aerosol optical properties and climate implications of emissions from traditional and improved cookstoves. *Environ. Sci. Technol*. **52,** 13647–13656 (2018).

15. Corbin, J. C. et al. Brown and black carbon emitted by a marine engine operated on heavy fuel oil and distillate fuels: optical properties, size distributions, and emission factors. *J. Geophys. Res. Atmos*. **123,** 6175–6195 (2018).
16. Wu, B., Wu, Z., Yao, Z., Shen, X. & Cao, X. Refined mass absorption cross-section of black carbon from typical non-road mobile machinery in China based on real-world measurements. *Sci. Total Environ.* **908,** 168579 (2024).
17. Yan, C. Q. et al. Characterization of carbon fractions in carbonaceous aerosols from typical fossil fuel combustion sources. *Fuel* **254,** 115620 (2019).
18. Olson, M. R. et al. Investigation of black and brown carbon multiple-wavelength-dependent light absorption from biomass and fossil fuel combustion source emissions. *J. Geophys. Res. Atmos.* **120,** 6682–6697 (2015).
19. Resquin, M. D. et al. Local and remote black carbon sources in the Metropolitan Area of Buenos Aires. *Atmos. Environ.* **182,** 105–114 (2018).
20. Targino, A. C., Krecl, P., Oukawa, G. Y. & Mollinedo, E. M. A short climatology of black and brown carbon and their sources at a suburban site impacted by smoke in Brazil. *J. Environ. Sci.* **136**, 498–511 (2024).
21. Mardoñez-Balderrama, V. et al. Atmospheric black carbon in the metropolitan area of La Paz and El Alto, Bolivia: concentration levels and emission sources. *Atmos. Chem. Phys.* **24,** 12055–12077 (2024).
22. Kouassi, A. et al. Measurement of atmospheric black carbon concentration in rural and urban environments: cases of Lamto and Abidjan. *J. Environ. Prot.* **12,** 855–872 (2021).
23. Peralta, O. et al. Atmospheric black carbon concentrations in Mexico. *Atmos. Res.* **230,** 104626 (2019).
24. Villalobos-Puma, E. et al. Atmospheric black carbon observations and its valley-mountain dynamics: eastern cordillera of the central Andes of Peru. *Environ. Pollut.* **355,** 124089 (2024).
25. Reyes, F. et al. Impact of Biomass Burning on Air Quality in Temuco City, Chile. *Aerosol Air. Qual. Res.* **21,** 210110 (2021).
26. Blanco-Donado, E. P. et al. Source identification and global implications of black carbon. *Geosci. Front.* **13**, 101149 (2022).
27. Xulu, N. A., Piketh, S. J., Feig, G. T., Lack, D. A. & Garland, R. M. Characterizing Light-absorbing Aerosols in a Low-income Settlement in South Africa. *Aerosol Air. Qual. Res.* **20**, 1812–1832 (2020).
28. Kalisa, E. & Adams, M. Population-scale COVID-19 curfew effects on urban black carbon concentrations and sources in Kigali, Rwanda. *Urban Clim.* **46,** 101312 (2022).
29. Curto, A. et al. Predictors of personal exposure to black carbon among women in southern semi-rural Mozambique. *Environ. Int.* **131,** 104962 (2019).
30. Djossou, J. et al. Mass concentration, optical depth and carbon composition of particulate matter in the major southern West African cities of Cotonou (Benin) and Abidjan (Cote d'Ivoire). *Atmos. Chem. Phys.* **18,** 6275–6291 (2018).

31. Guo, B. et al. Long-term variation of black carbon aerosol in China based on revised aethalometer monitoring data. *Atmosphere* **11,** 684 (2020).
32. Dao, X. et al. Significant reduction in atmospheric organic and elemental carbon in $PM_{2.5}$ in 2+26 cities in northern China. *Environ. Res.* **211,** 113055 (2022).